Sánchez-García, E.; Palomar-Vázquez, J.; Pardo Pascual, JE.; Almonacid-Caballer, J.; Cabezas-Rabadán, C.; Gómez Pujol, L. (2020). An efficient protocol for accurate and massive shoreline definition from mid-resolution satellite imagery. Coastal Engineering. 160:1-15. https://doi.org/10.1016/j.coastaleng.2020.103732

An efficient protocol for accurate and massive shoreline definition from mid-resolution satellite imagery

E. Sánchez-García [a*], J.M., Palomar-Vázquez [a], J.E. Pardo-Pascual [a], J. Almonacid-Caballer [a], C. Cabezas-Rabadán [a], L. Gómez-Pujol [b]

[a] Geo-Environmental Cartography and Remote Sensing Group, Department of Cartographic Engineering, Geodesy and Photogrammetry, Universitat Politècnica de València, Camí de Vera, s/n 46022, Valencia, Spain

[b] Earth Sciences Research Group, Department of Biology, University of the Balearic Islands, Ctra. Valldemossa, km 7.5, 07122 Palma, Balearic Islands, Spain

* Corresponding author. *E-mail address*: elena.sanchez.upv@gmail.com

Abstract

Satellite images may constitute a useful source of information for coastal monitoring as long as it is possible to manage them in an efficient way and to derive precise indicators of the state of the beaches. In the present work, SHOREX system is employed for managing and processing Landsat 8 and Sentinel 2 images to automatically define the instantaneous shoreline position at sub-pixel level. Between the years 2013 and 2017, 91 satellite-derived shorelines (SDS) were assessed by comparing with high-resolution shorelines obtained simultaneously through video-monitoring. The analysis allowed identifying the combination of parameters to perform the extraction algorithm with the highest accuracy. Furthermore, an efficient self-contained workflow is proposed, more robust and independent from inaccuracies in the approximate input line and from multiple morphological and oceanographic issues that may condition the radiometric response near the shore. An iterative procedure ensures firstly a suitable kernel of analysis representing the water-land interface to get, afterward, the definition of the sub-pixel shoreline with high accuracy (below 3 m RMSE).

Keywords: sub-pixel shoreline mapping, coastal monitoring, beach changes, Landsat 8, Sentinel 2, video-monitoring, SHOREX.

1. Introduction

Beaches are spaces of great environmental and recreational importance for coastal societies. The characterization of their state and morphological changes, such as shoreline monitoring, is of special interest for the subsequent management of the coast (Mills et al., 2005, Esteves et al., 2009, Addo et al., 2011, Alharbi et al., 2017). In order to meet monitoring and management needs, data collection must offer enough accuracy and frequency. Among the methods traditionally used, photointerpretation is limited to provide data at specific times (Ford, 2013; Jones et al., 2009; Morton et al., 2004; Pajak & Leatherman, 2002). Similarly, more modern and continuous video-based techniques are limited to a local scale (Aarninkhof et al., 2003; Davidson et al., 2007; Taborda & Silva, 2012; Brignone et al., 2012; Simarro et al., 2017; Sánchez-García et al., 2017), while DGPS requires arduous in-situ data acquisition (Pardo-Pascual et al., 2005; Psuty & Silveira, 2011).

Alternatively, satellite images can provide information of the entire planet with high temporal frequency. In 2008, NASA released the images of the Landsat platform (16 days of revisit time) free of charge. Similarly, the European Spatial Agency (ESA) is providing the Sentinel-2 satellite images (5 to 10 days of revisit time). Nowadays, considering both platforms together, there is a global average revisit interval of 2.9 days (Li & Roy, 2017). Thus, there is a new scenario where the shoreline position may potentially be defined in tens of different dates throughout the year along broad coastal segments. This type of data may make it possible to characterize short-term coastal processes such as the effect of storms and their subsequent recovery over time, as well as the impact of beach nourishments or coastal protection works (Cabezas-Rabadán et al., 2018; 2019a, b). However, in order to take advantage of these images it is necessary to: (i) define the shoreline position with enough accuracy for recognizing subtle changes, and (ii) have a sufficiently efficient and automated system to define the shorelines of all the images acquired by the satellites in a low time consumption process.

Near and medium infrared bands have been commonly used to detect the interface between water and land (Frazier & Page, 2000; Ryu et al., 2002; Yamano et al., 2006; Maiti & Bhattacharya, 2009). Similarly, alternative strategies have been proposed such as combining bands for obtaining indexes (Ouma &

Tateishi, 2006, Choung & Jo, 2015). Among these indexes, the first and most used is the Normalized Difference Water Index (NDWI) that combines the green band with the near-infrared band using the zero value as a threshold for the difference between the dry sand and wet ocean surface (McFeeters, 1996). Xu (2018) proposed the Modified Normalized Difference Water Index (MNDWI), which replaces the near infrared band with the SWIR 1. Subsequently, new proposals have appeared such as the Automated Water Extraction Index (AWEI), which combines different bands of the visible and near and medium infrared but applying different weights to each band (Feyisa et al., 2014). These automatic water classifications have always encountered problems according to the index employed, as well as to the specific threshold chosen that varies with the different scenes and places (Ji et al., 2009). On the other hand, these indexes often confuse water zones with low albedo covers (Feyisa et al., 2014). Therefore, there is no clear consensus on which index works best as most authors focus on the correct performance of the index in their area of study. Rokni et al. (2014) evaluated multiple indexes to estimate surface changes in Lake Urmia (Iran) and found that the best solution came from a new approach based on the main components of NDWI. Hagenaars et al. (2018) used the NDWI to automate the shoreline definition, although in this case, grouping the water spots into a single large unit associated with the sea and separating it from the land. More recently, Viaña-Borja & Ortega-Sánchez (2019) proposed new water indexes to map the shoreline position using surface reflectance rather than top-of-atmosphere reflectance from blue and SWIR 2 Landsat bands, whereas Vos et al. (2019b) integrated a supervised image classification procedure based on a particular neural network classifier.

In the attempt to automatically define the shoreline from mid-resolution satellite images using the raw infrared bands, the strategies appear divided in those working on a pixel scale, and those trying to improve the precision beyond the pixel size (sub-pixel or super-resolution). In the first case, the location of the shoreline is determined by an optimal threshold (Aedla et al., 2015; Quang Tuan et al., 2017, Song et al., 2019), as well as by the selection of optimal bands and a subsequent classification (Li & Damen, 2010; García-Rubio et al., 2015, Vos et al., 2019b). However, detailed coastal analyses would require the definition of the shoreline at sub-pixel level, improving the excessively coarse spatial resolution of the input satellite images. A few works have proposed algorithms in order to overcome that restriction (Foody et al., 2005; Zhang & Chen, 2010; Li & Gong, 2016, Li et al., 2015; Liu et al., 2017a). Nevertheless, most of these solutions focus on the algorithm basics, but without proposing any specific method to ensure a sufficiently robust georeferencing. This is a key issue considering that NASA and ESA images show an excessive uncertainty in geolocation. Landsat 8 L1T products require an uncertainty lower than 12 m (Iron et al., 2012) while with regard to the multi-temporal registration, the geolocation accuracy has been previously established in 1.2 pixels, i.e. 24 m (Clerc, 2017). Hence, automatic co-registration methods appear as necessary in order to ensure a minimum error. Almonacid-Caballer et al. (2017) proposed employing the Local Upsampling Fourier Transform, LUFT algorithm (previously described by Guizar-Sicairos et al., 2008 and Wang et al., 2011), as a useful tool for this purpose since it ensures an error below 1/10 of the pixel resolution.

The methodology initially proposed by Pardo-Pascual et al. (2012) and later improved by Almonacid-Caballer (2014), includes both an automatic shoreline extraction algorithm and an automatic co-registration system, both at sub-pixel level. This algorithm, which works on the near- and mid-infrared spectral band, is a potentially usable methodological solution to automatically extract multiple shorelines as Pardo-Pascual et al. (2018) assessed. For each image, the method follows three essential steps. First, the approximate location of the shoreline at pixel level is defined based on threshold techniques. Second, sub-pixel definition is determined automatically based on the location of maximum gradient points.. They are obtained adjusting a polynomial function to the digital levels of a 7 x 7 kernel (neighborhood of analysis) around each pixel of the approximate line and subsequently detecting the position where the Laplacian is null. Lastly, a geometric correction is performed based on LUFT. Previous results on rigid coasts -seawalls- showed accuracies close to 5 m RMSE (Pardo-Pascual et al., 2012), while on microtidal sandy beaches the values were somewhat higher: 6.6 m for Landsat 8 (L8) and Sentinel 2 (S2) images and slightly worse for Landsat 7 (Pardo-Pascual et al., 2018), always experiencing a clear bias towards the sea. This bias was previously detected by comparing the shorelines obtained from Landsat 5 and 7 images against others derived from more precise systems such as DGPS and LiDAR (Almonacid-Caballer et al., 2016). Pardo-Pascual et al. (2018) and Hagenaars et al. (2018) also found that the accuracy may be strongly influenced by wave conditions as the foam and the wave period.

It was thought that the persistence of this bias could be minimized by working with smaller kernels. However, at once, the inaccuracy of the initial approximate shoreline defined by threshold techniques (first step) required sufficiently large kernels to ensure that the real shoreline was contained in the kernels analyzed during the sub-pixel extraction (second step). Moreover, the use of threshold techniques impeded a complete automation of the process. Considering the variability of elements existing in the marine area, it is very difficult to find a single proper threshold for every image as Liu et al. (2011) and Almonacid-Caballer (2014) previously stated.

Although the methodological basis described in Pardo-Pascual et al. (2018) is a good starting point, it cannot be considered as an efficient solution for working with large sets of satellite images. For that purpose, Palomar-Vázquez et al. (2018a, b) proposed to replace the pixel level lines defined by thresholding techniques by a unique approximate line for the whole set of images. The approximate line can be then obtained either from a pre-existing cartographic source or from a coarse photo-interpretation on an orthophoto close in time to the studied period. It increases the efficiency of the overall process by excluding the single step that required user intervention. This modification allows designing an automatic shoreline extraction system, which we have called SHOREX (Shoreline Extraction), able to supply updated shorelines from the images systematically acquired by the satellites L8 and S2.

The accuracy of the final sub-pixel shoreline is related both to the size of the kernel of analysis and to the degree of the adjusted polynomial (second step). Although remaining uncertain, the approximate shoreline obtained according to the new workflow is expected to be more robust and may allow a reduction of the kernel of analysis. This modification, in turn, would allow changing the degree of the adjusted polynomial, potentially offering higher accuracies when determining the shoreline position. At this point, it seems also necessary to re-evaluate the data sources to be used as input for the SHOREX process. The performance of the Infrared bands (NIR, SWIR1, SWIR2) must obviously be tested but also the NDWI index proposed in the literature.

The use of a single approximate line to start the process presents certain challenges to be solved. If this line was excessively displaced with respect to the real shoreline − either because of a wrong delineation or because there have been significant changes between the acquisition dates of the approximate line and the satellite image − when using a small analysis kernel the system may not find the real land/water limit. Therefore, it would be very useful to analyze the effect that an inadequate displacement of the approximate line can have on the system, as well as to propose possible solutions to provide methodological robustness.

This paper aims to present SHOREX as an automatic shoreline extraction system from mid-resolution satellite imagery. The optimum combination of parameters of the extraction algorithm (kernel size and polynomial degree) for achieving the highest accuracy is identified on the microtidal beach of Cala Millor, as well as an assessment of the results when using as input different bands or indexes. It is also intended to evaluate whether the position of the approximated line affects the precision of the final sub-pixel shoreline. Once the optimum parameters and input data have been determined, the aim is to define an operative and self-reliant shoreline extraction protocol from L8 and S2 images. The method is expected to release the demands on the initial solution and be more robust against external factors.

2. Study area

Cala Millor is a semi-embayed microtidal sandy beach, 1.7 km in length, located on the northeastern coast of Mallorca (Balearic Islands, Western Mediterranean –see Fig. 1). Well-sorted medium to coarse biogenic carbonate sand characterizes the beach bottom from shoreline to 6 m in depth (Gómez-Pujol et al., 2007). Seawards from this point, the endemic *Posidonia oceanica* seagrass meadow carpets the bottom (Infantes et al., 2012). This is an intermediate beach with a highly dynamic configuration of sinuous-parallel bars and troughs, presenting intense variation in the bathymetry and shoreline position related to sandbar movement (Álvarez-Ellacuría et al., 2011; Gómez-Pujol et al., 2011).

Tides are almost negligible with a spring tidal range below 0.25 m, although changes in atmospheric pressure and wind stress can account for a considerable portion of sea level fluctuations (Gomis et al., 2012). The Balearic Sea, the most western basin of the Mediterranean Sea, is a semi-enclosed and calm sea with a relatively moderate wave condition. The beach is open to the east and, due to the embayment configuration; it is well exposed to waves from the NNE to the SE (Enríquez et al., 2017). Significant wave height (H_s) at deep waters is usually below 0.9 with the peak period (T_p) between 4 and 7 s.

However, frequent storms account for 2% of the time and increase H_s up to 5 m with Tp higher than 10 s, with a return period of 1.5 years (Tintoré et al., 2009).

This beach is an important tourist resort of the eastern coast of Mallorca with more than 60000 visitors during the summer period and a long history of sand nourishment and coastal management approaches (Tintoré et al., 2009). Since November 2010 the Balearic Islands Coastal Observing and Forecasting System (SOCIB) has been monitoring Cala Millor Beach by means of coastal video-monitoring and seasonal beach profiling and an annual bathymetry and sediment sampling (Tintoré et al., 2013).

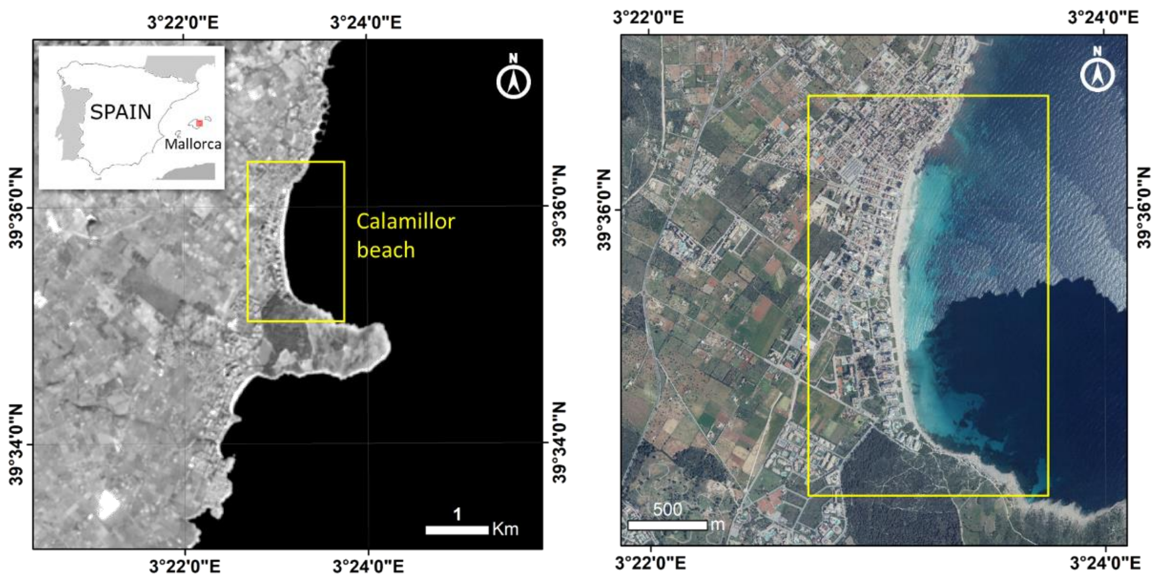

Fig.1. Location map of the study area in the Balearic Islands (Western Mediterranean).

3. Materials and methods

The whole set of satellite-derived shorelines (SDS) resulting of applying SHOREX through the different combination of parameters (kernel size, polynomial degree and input band) were assessed by comparing them against more accurate shorelines. The latter ones were obtained from images captured by the SIRENA video-monitoring system (Nieto et al., 2010) and being later, processed and converted to georectifed images by applying C-Pro (Sánchez-García et al., 2017). The assessment includes shoreline data of 91 instants registered using both satellite and video sources (from 12 June 2013 to 23 May 2017) over almost 4 years (Fig. 2), and defined as the time-varying interface between water and dry sand (Boak and Turner, 2005).

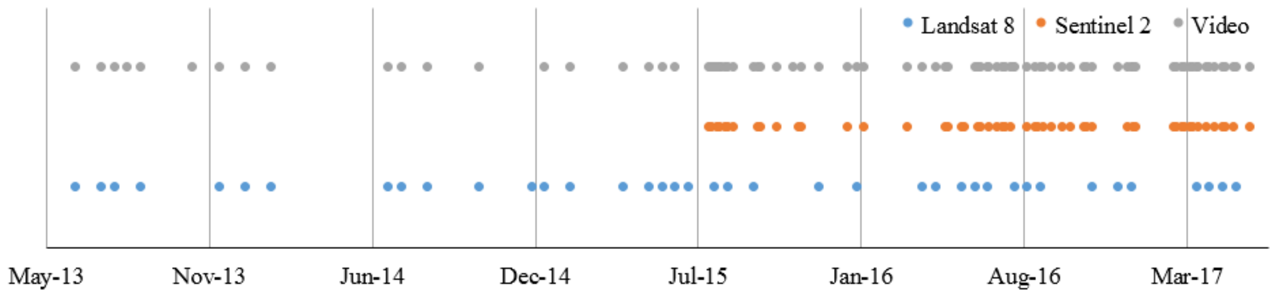

Fig. 2. Temporal distribution of the 91 satellite images (L8 and S2) and the simultaneous 85 video-camera images used for the assessment. The discrepancy in the number of data between satellite and video is because there are 6 days with images of both satellites.

3.1. Reference data from video-monitoring

The shore-based video system (SIRENA), part of the SOCIB program, is equipped with some CCD cameras continuously covering and monitoring the whole view of Cala Millor Beach from an elevation of 46.5 m. Fig. 3 presents the field of view covered by the four cameras used for the study. The remote station stores hourly images with a resolution of 1280 x 960 pixels, with a frequency of 7-5 fps during a roughly 10-minute span. This way, mean images (widely known as timex images –Holman & Stanley, 2007– and used for a long-term monitoring of shoreline change –Ruiz de Alegria-Arzaburu &Masselink, 2010) are generated showing the patterns of high-frequency variability. In this work, 85 timex at 10 am (UTC time) for each camera −closest time to the satellite passage− are selected as reference data to assess the SDS.

Fig. 3. Timex images of 7/02/2014 at 10 am UTM time and acquired from left to right by C1, C2, C4 and C5 cameras.

Before georectifying the video-camera images, other pre-processing tasks are required to ensure their quality such as distortion corrections and the registering between images due to obvious camera displacements over time. Ten ground control points (GCPs) for each photographic shot were measured by the SOCIB to have control of the video-monitoring system.

Firstly, the correction of the distortions inherent to each camera device is overcome by using the Camera Calibration Toolbox (Bouguet et al., 2015), which allows the calibration parameters to undistort the images that mainly suffered from radial and tangential distortion. The image coordinates of the GCPs also had to be transformed since they were identified on the distorted image.

Secondly, in order to check the displacement between images over time, a set of stable and recognizable points available in the two images are identified (buildings, windows, contours of distant mountains, etc.). Then, the same points located at the control image are found in the rest of the images through a cross-correlation search process. The homologous points are used to derive the affine transformation parameters through least squares. However, the main part of the correction corresponds to a translation in both x and y-axis of the image space as figures 4A and 4B evidence. The standard deviation estimator of the least square adjustment is known for each image and, in average for the whole set of photos and the four cameras, is 0.56 pixels and 0.65 pixels along the x and y-axis respectively.

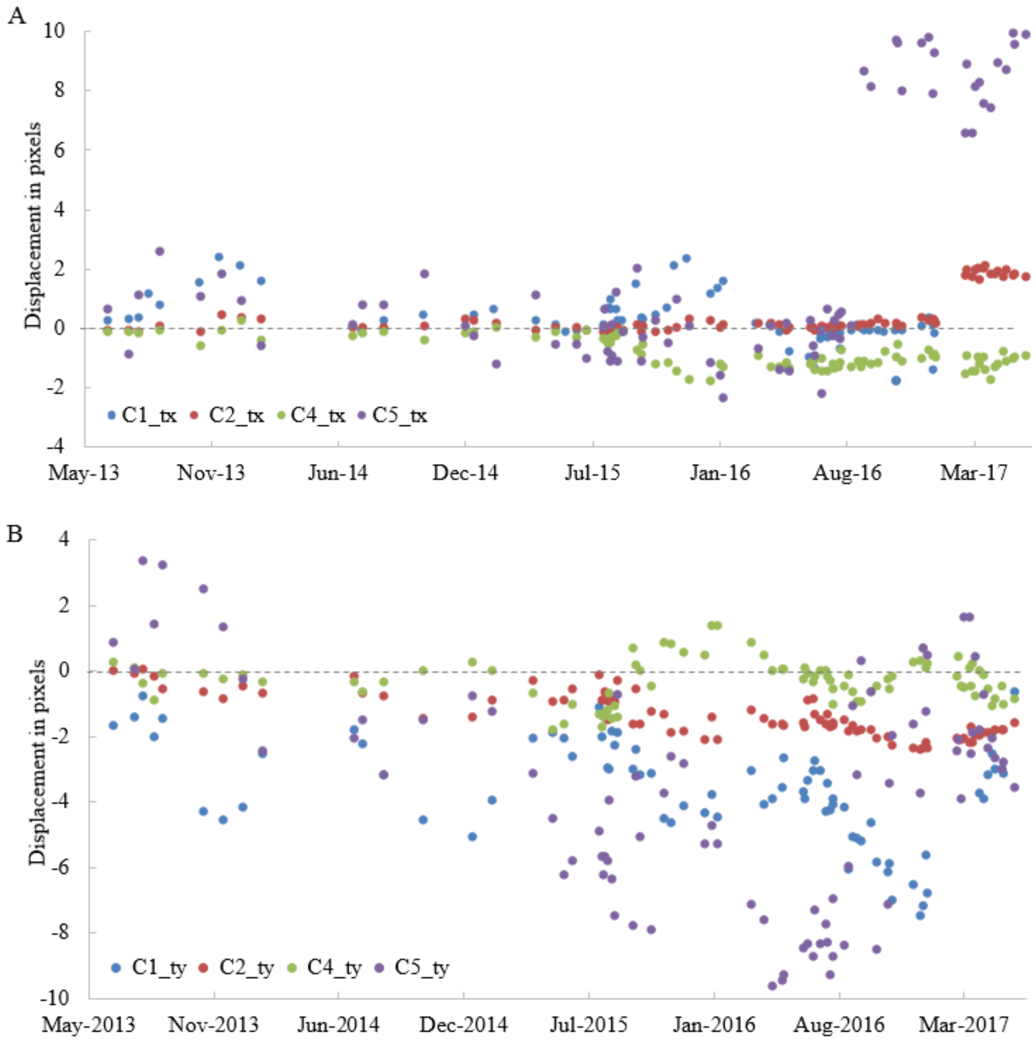

Fig. 4. Displacement occurred in the positioning of the four cameras (C1, C2, C4 and C5) during the study period along the x-axis in Fig. 4A, and along the y-axis in 4B. The graphic representation scale collects the most of the results but note that there are extreme values going out of it.

Most of the measured displacements over the period range in the x-axis within ±3 pixels for the four cameras as Fig. 4A shows. However, C1 reaches an extreme displacement in the x-axis up to -112.29 pixels in February 2017, and C5 moves in the opposite direction up to 11.82 pixels from September 2016 (see that both data sets disappear from the graph area). Some of these changes have a progressive character as exemplifies C1 but others are sudden such as those occurred in C2 between January and February 2017 (outside the graphic representation scale).

Regarding the general movement occurred in the y-axis, Fig. 4B describes clear differences regarding the stability of the four cameras. Again, the ones located at the ends are the most unstable. It is exemplified by

C1 as it reached up to -76 pixels of displacement associated with the episode of February 2017 and until it was settled in April 2017 (extreme errors that do not appear in Fig. 4B but are shown in Fig. 5). The overall correction values in y-axis indicate that cameras are clearly experiencing displacements over time.

This pre-processing analysis justifies the georeferencing campaigns carried out by the SOCIB in order to calibrate the video-monitoring system and allowing its use despite the setbacks. However, in this work, we bet to overcome the problem of the camera displacements by registering every photo against a control image that we choose on 11/06/2014 −when the closest georeferencing campaign to the 4-year study period was done.

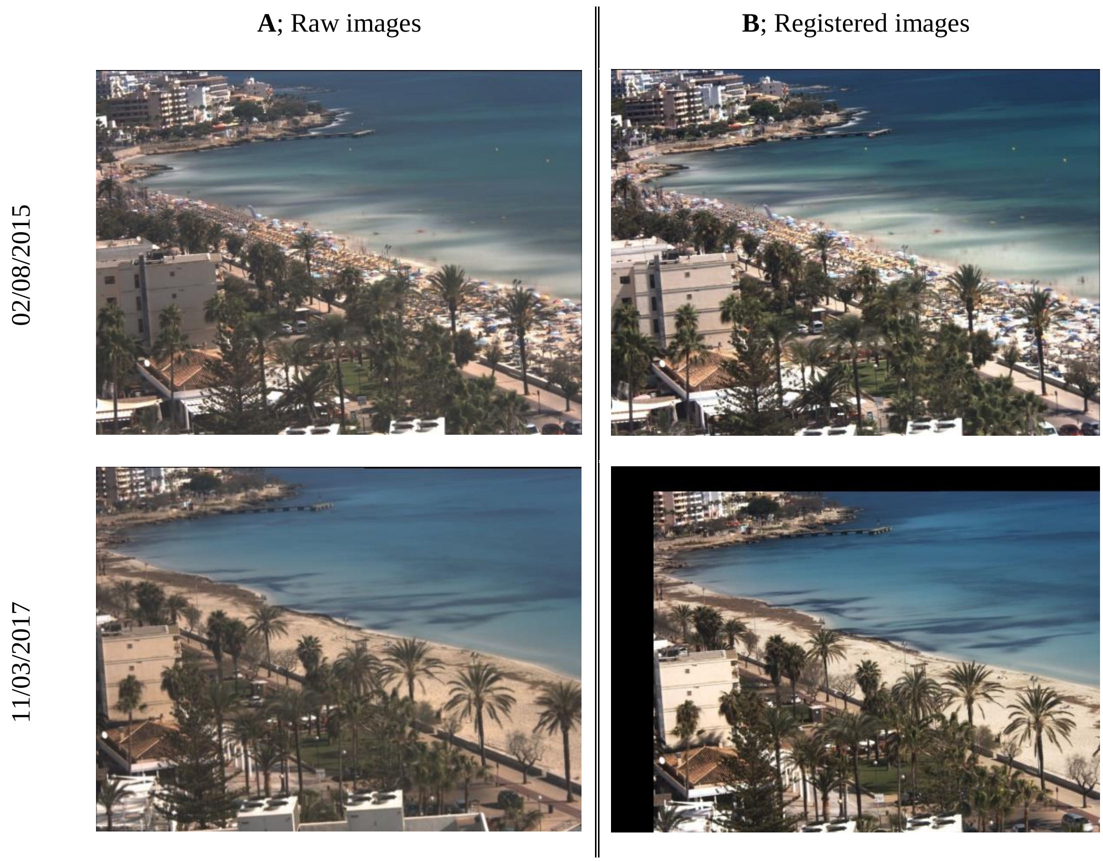

Fig. 5. Displacement occurred in C1 between two dates: top panels represent the images registered on 02/08/2015, and bottom panels represent the images on 11/03/2017 (19 months later). Fig. 5A, on the left, shows the raw images stored by SIRENA. After registering them against the control image on 11/06/2014, the displacement is quantified in 0.6 and -1.95 pixels in the x and y-axis for the top-left image, and -111.12 and -65.79 pixels in the x and y-axis for the bottom-left image. Fig. 5B, on the right, shows the images after the registration process (free of displacements), where a certain pixel for the whole set of images will correspond over time with the same terrain value.

Once the registration process is done, the GCPs, corresponding with non-fixed points identified for their associated field campaign, can be manually identified only once in the control image −with expected errors within the pixel level. Thus, the camera intrinsic and extrinsic parameters are determined in one go (Sánchez-García et al., 2017) and the georectification for the whole set of images over the 4-year study is carried out using C-Pro tool.

Note that the spatial resolution of the georectified image is a limitation to consider. Despite the proper elevation of the camera above 40 m sea level, and with a focal length ranging for the four cameras between 5060 to 1332 pixels, the pixel resolution at 1 km would range 0.2 m to 0.7 m in the cross-shore footprint component and 4.2 m to 15 m in the long-shore component. Large focal lengths lead to better resolutions and the obtained values are in line with Holman & Stanley (2007).

The photos are projected above a sea level value obtained from the tide gauges closest to Cala Millor (Sa Rapita, Pollença and Andratx –see 'http://www.socib.eu/?seccion=observingFacilities&facility=mooring'). Combining these three tide data gauges and for each particular date, the available sea level data was averaged out the 10 minutes coincident with the register of the timex image. The accuracy reached for the resection process was assessed by projecting 43 GCPs over its particular elevation value as Fig. 6 shows, and getting an RMSE of 1.54 m (promising results similar to those obtained by Sánchez-García et al., 2019b and Taborda & Silva, 2012).

To end the process, the shoreline is digitalized from the georectified timex images as that feature designing the water-land edge between both interfaces (Fig. 6 exemplifies this procedure). The benefit of using timex for shoreline detection is proved in several works (Aarninkhof et al., 2003; Álvarez-Ellacuría et al., 2011; Osorio et al., 2012; Valentini et al., 2017). The resulting 85 video-derived shorelines will act as a reference to assess the ones obtained from satellite imagery.

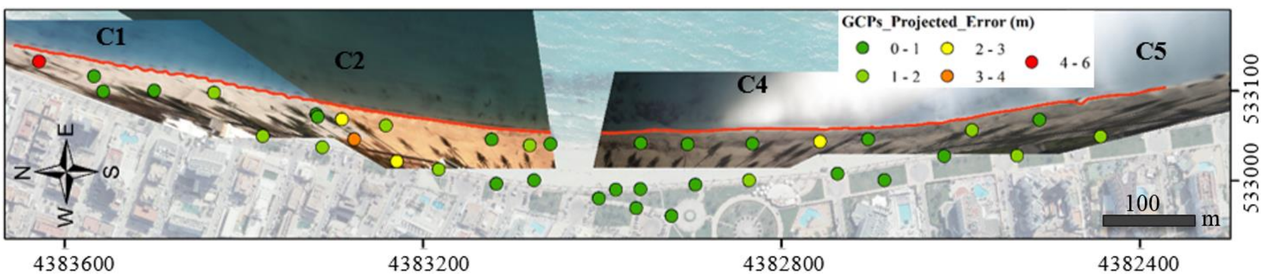

Fig. 6. Projection map with the georectified photos of 7/02/2014 (corresponding oblique photos of Fig. 3) for Cala Millor beach shown over an orthophoto taken from 2010 PNOA sources (Spanish National Program for Aerial Orthophoto). The map shows the digitalized shoreline (red line) and the projection error calculated on the GCPs. The projection is made above the sea level value as near in time with the photos as possible. Grid coordinates: GCS_ETRS89 UTM 31.

3.2. Shoreline definition from Landsat 8 and Sentinel 2 imagery

The definition of the SDS was carried out with SHOREX from mid-resolution satellite images. It is a shoreline extraction system that includes as its core the algorithmic solution for the extraction with sub-pixel precision proposed in Pardo-Pascual et al. (2012) and Almonacid-Caballer (2014). Surrounding it, a workflow has been developed in order to integrate and automatize all the necessary operations to efficiently manage a large volume of raw data: the satellite images of L8 and S2 with a resolution of 30 m and 20 m respectively.

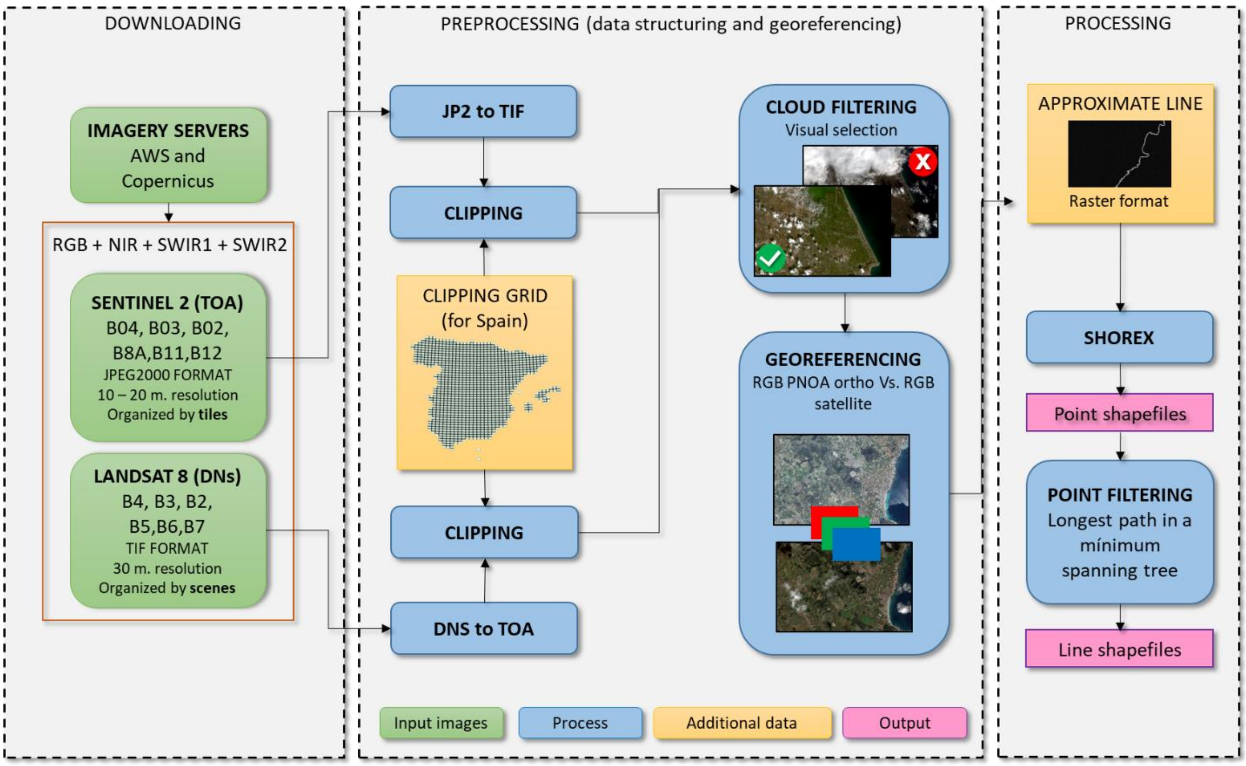

Fig. 7. The SHOREX workflow consists of three phases: (1) downloading, (2) pre-processing and (3) processing.

A set of separated tools have been integrated within a single Python framework, following the workflow of Fig. 7 and previously described in Palomar-Vázquez et al. (2018 a, b) where the efficiency of the extraction protocol (time consumption) and its limiting factors are analyzed. The entire computational time to obtain the 91 shorelines of Cala Millor Beach is estimated in 5.05 h, of which 67% of the time corresponds to the downloading, 8.6% to the pre-processing and 24.4% to the processing. The first phase, downloading the bands of interest, is carried out free of charge from Amazon Web Services (AWS) for L8 and COPERNICUS server for S2. These servers provide API methods which allow the download of a massive number of images with a high degree of flexibility and automation. Thus, by means of using a scripting language like Python, it is possible to individually download the required bands for a specific project. The second phase, the preprocessing, prepares each band for the analysis. For this purpose, several tasks are included: image format conversion, clipping each scene in smaller tiles (to improve the storing and shorten the time processing), TOA (top of atmosphere) reflectance conversion, cloud filtering for discarding useless images, and band sub-pixel georeferencing according to the method proposed by Guizar-Sicairos et al. (2008) and modified by Almonacid-Caballer et al. (2017) to work as phase-correlation. The last phase, the processing, consists of the definition of the shoreline position at sub-pixel level. It needs as input both the pre-processed band to be analyzed and an initial approximate shoreline in raster format. For every single pixel of the initial shoreline, SHOREX performs an analysis of the kernel and detects the shoreline position at sub-pixel level. It is important to emphasize that the approximate line is used to process all bands and dates so decreasing the processing time, instead of using a manual thresholding process for every band as previous works did (Almonacid-Caballer et al., 2016, Pardo-Pascual et al., 2018). Moreover, a suitable value selection in the parameters controlling the algorithm, such as the kernel size and the degree of the surface polynomial function, is essential for a correct determination of the shoreline position. Fig. 8 exemplifies the procedure carried out by the algorithm in the search for the sub-pixel shoreline in a particular 7x7 kernel and through a fifth-degree polynomial surface.

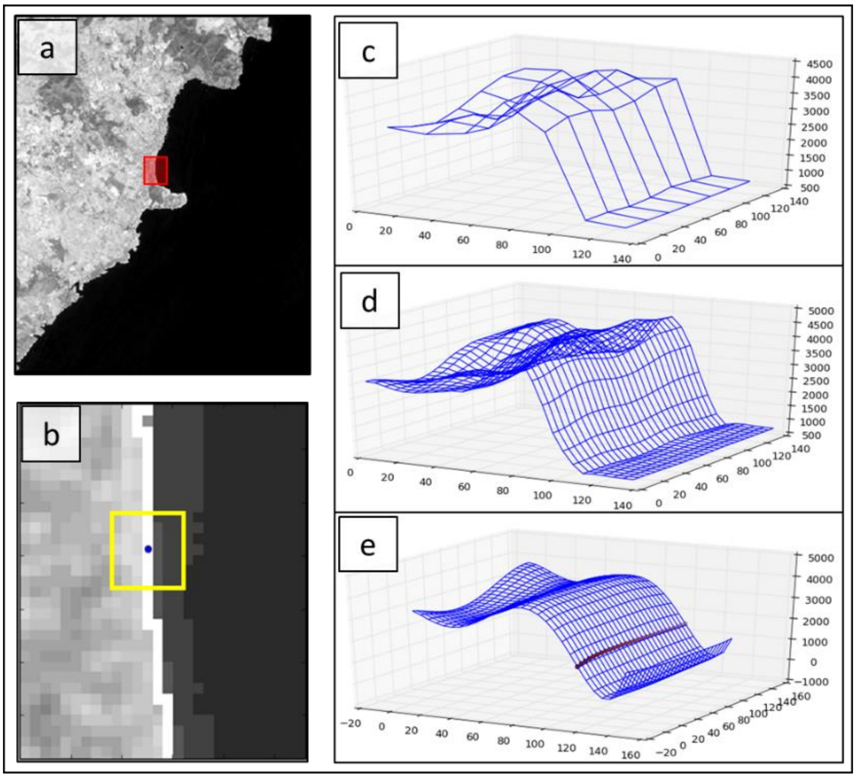

Fig. 8. Core algorithm of SHOREX. a) Band SWIR1 of S2 for the study area; b) initial approximate line (in white color) and a7x7 kernel of analysis (yellow color); c) 3D display of the kernel values; d) 3D display of the resampled kernel values; e) fifth-degree polynomial surface fitted to the resampled values with the extracted sub-pixel shoreline.

Once the shoreline points have been obtained as Fig 8e shows, it is possible that several outliers appear (for instance, due to the presence of buildings or vegetation near to the beach). In order to avoid them, a point filtering method has been implemented based on the minimum spanning tree algorithm (MST) (Graham & Hell, 1985). In this way, the MST is computed for the shoreline points and, subsequently, those of the longest path are selected, as they potentially belong to the shoreline as Fig. 9 shows. The result is a shapefile with the SDS in either points or polyline format.

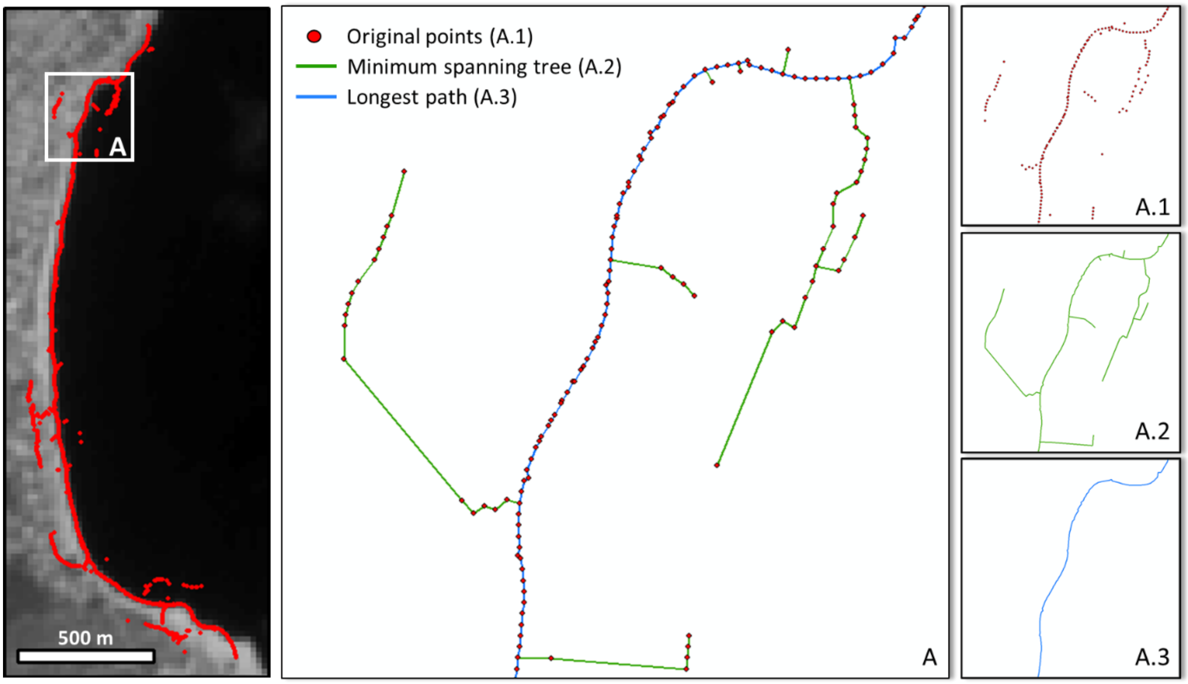

Fig. 9. Example of applying the MST process in the final step of SHOREX algorithm to remove outlier points from the SDS. The longest path of the MST (A.3 solution) will shape the sub-pixel shoreline.

3.3. Accuracy tests

At this point, different sets of shorelines were obtained from L8 and S2 imagery by modifying the parameters of the methodology of extraction. For each combination of parameters, the accuracy of the 91 SDS was defined by comparing their position with the associated reference lines simultaneously obtained from video-monitoring. For each set of results containing shorelines from different dates, the mean bias, the standard deviation, and RMSE were calculated, and they were used to assess the accuracy of each combination of parameters. Positive and negative differences mean that the SDS is displaced seawards and landwards respectively.

-Test 1: Combination of different kernels, degree of the polynomial and input bands

The first test consists in finding the combination of parameters and inputs to the shoreline extraction process that offers the highest accuracy. As the position of the final sub-pixel shoreline is related both to the degree of the adjusted polynomial and to the size of the analyzed kernel, these parameters have been modified in the extraction process. With this purpose, 84 different combinations were tested over 91 images, 39 for L8 and 52 for S2 images as Table 1 summarizes.

Table 1. Combination of parameters for test 1.

Platform	Number of dates	Processed bands	Degrees	Kernels of analysis (pixels)
L8	39	NIR, SWIR1, SWIR2, NDWI	3, 4, 5	3X3, 5X5, 7X7
S2	52	NIR, SWIR1, SWIR2, NDWI	3, 4, 5	3X3, 5X5, 7X7, 11X11

With regard to the kernel, the maximum size used for L8 was 7x7 (210 x 210 m), while the maximum kernel for S2 images was 11x11 (220 x 220 m). This decision was taken in order to cover an equivalent surface in both types of images considering the different spatial resolutions.

Similarly, the input data sources were re-evaluated. The infrared bands (NIR, SWIR1, SWIR2) that have offered the best results in previous studies (Pardo-Pascual et al., 2018) were tested. At the same time, the performance of the index NDWI was also assessed to know if it could provide good results as it is presented in the literature as an adequate solution (Rokni et al., 2014; Hagenaars et al., 2018).

-Test 2: Assessing the effects caused by an inaccurate input shoreline

The robustness of the system was checked when employing an approximate pixel level line excessively displaced from the position of the real shoreline. In order to do this, the approximate line was synthetically shifted one pixel to each side (landward and seaward), and the positions of the resulting shorelines were analyzed.

The proposal of an iterative process when facing an eventual inaccurate pixel level shoreline is assessed. This way, the accuracy of the final shoreline is untied from previous matters. In order to ensure that the appropriate pixels cover the water-land surface, a larger kernel is initially suggested for the analysis to proceed afterward with the second extraction process (refining) through a smaller kernel with which to achieve sub-pixel precision. The shoreline extracted in the first iteration is the one used as input for the second one. It will be analyzed if the result of this latter iteration is convergent with the solution obtained when using an appropriate approximate line since the first moment.

4. Results

4.1. Combination of different kernels, degree of the polynomial and input bands

Test 1 attempts to determine the best combination of parameters to extract the most accurate sub-pixel shoreline, assuming that the initial approximate line is accurate enough to be contained in the analysis kernels. Every combination of parameters for each processed band and platform is assessed. Fig. 10A summarizes the mean and the standard deviation values achieved by working with 39 images of L8, and 52 images of S2. Firstly, it is possible to observe that the NDWI band generally offers worse results than the pure bands, considering both the mean and the standard deviation. At the same time, when analyzing the RMSE value resulting from each combination of parameters (Table 2) it is easier to confirm that the best results for L8 are achieved by using the SWIR1 band, a 3x3 kernel and a third-degree polynomial, obtaining an RMSE of 3.57 m. Similarly, for S2 the best choice comes from the SWIR1 band and a third-degree polynomial, but using a 5x5 kernel (equivalent solution according to the differences in spatial resolution), obtaining 3.01 m RMSE. Working with these combinations of parameters, the algorithm is able to define the shoreline with an error of 0.07±3.57 m for L8 and 1.33±2.7 m for S2 (see Fig. 10A).

Table 2. RMSE values (in meters) resulting from applying SHOREX for the 84 different combinations of parameters (36 and 48 solutions for L8 and S2 respectively). The values in bold highlight the best solutions.

		LANDSAT 8			SENTINEL 2			
Bands	Degree\kernel	3	5	7	3	5	7	11
NIR	3	3.82	15.18	19.39	7.26	7.99	7.33	13.05
	4	11.29	17.78	18.07	3.71	8.22	8.27	16.44
	5	12.96	18.52	18.06	3.69	4.57	9.65	29.97
SWIR1	3	**3.57**	6.23	11.57	7.13	**3.01**	10.59	10.96
	4	11.51	8.52	15.84	3.25	3.93	8.57	16.09
	5	13.16	6.20	18.69	3.11	6.84	3.64	23.76
SWIR2	3	3.69	14.83	12.02	7.14	3.14	10.47	11.73
	4	11.52	8.38	15.59	7.66	4.70	10.54	18.70
	5	13.28	6.40	13.93	9.75	7.25	4.08	25.10
NDWI	3	12.62	8.81	9.71	7.07	7.90	7.70	11.37
	4	15.67	15.05	17.45	8.83	12.24	13.62	16.50
	5	15.23	16.42	16.15	8.36	9.60	10.60	17.00

4.2. Synthetic displacement of the approximate line

The previous test determines the best combination of parameters assuming an initial approximate line properly located in space. Nevertheless, it is essential to define to which extent a displacement of the initial line affects the resultant shoreline. Therefore, test 2 consists on repeating test 1 but synthetically shifting the initial approximate line one pixel to each side of its original position ‒meaning 30 m of displacement in L8 and 20 m in S2. Figures 10 and 11 represent the accuracy results when applying a displacement both landwards and seawards.

			LANDSAT-8 MEAN			LANDSAT-8 STANDARD DEVIATION			SENTINEL-2 MEAN				SENTINEL-2 STANDARD DEVIATION			
	Band	D \ K	3	5	7	3	5	7	3	5	7	11	3	5	7	11
A WHITHOUT DISPLACEMENT	NIR	3	1.59	4.72	8.95	3.48	14.43	17.20	1.20	2.79	5.53	9.71	7.16	7.49	4.81	8.72
		4	-0.00	1.53	5.58	11.29	17.72	17.19	0.93	2.05	4.79	12.84	3.60	7.97	6.75	10.28
		5	0.20	2.83	7.79	12.96	18.31	16.30	0.97	1.72	3.49	8.36	3.56	4.24	9.00	28.79
	SWIR1	3	0.07	4.75	9.55	3.57	4.03	6.54	0.17	1.33	5.20	10.20	7.13	2.70	9.23	4.03
		4	-1.61	0.93	6.11	11.40	8.47	14.63	-0.98	-0.34	2.67	13.64	3.11	3.92	8.14	8.54
		5	-1.43	2.09	5.72	13.09	5.84	17.80	-0.75	-0.23	1.91	9.73	3.02	6.84	3.10	21.68
	SWIR2	3	-0.21	4.41	9.67	3.69	14.17	7.15	-0.81	0.35	4.87	9.88	7.10	3.13	9.27	6.34
		4	-1.86	0.63	6.01	11.38	8.36	14.39	-2.35	-1.95	1.27	13.33	7.30	4.28	10.47	13.13
		5	-1.68	2.01	5.69	13.18	6.09	12.72	-2.09	-1.36	1.05	11.09	9.53	7.13	3.95	22.53
	NDWI	3	6.99	7.30	6.95	10.52	4.94	6.80	5.92	5.70	5.23	6.64	3.88	5.48	5.65	9.23
		4	7.78	8.51	8.21	13.61	12.41	15.40	7.44	9.13	8.85	9.04	4.78	8.16	10.36	13.81
		5	7.60	7.64	7.46	13.21	14.54	14.33	7.10	7.16	6.56	6.40	4.42	6.40	8.33	15.76
B 1 PIXEL SEAWARDS	NIR	3	17.00	29.88	14.56	8.03	39.84	20.85	11.57	1.39	7.99	16.39	9.50	15.66	10.34	8.45
		4	18.53	5.50	4.50	12.30	14.21	14.31	11.58	-0.47	-1.47	0.00	9.63	6.21	8.55	12.64
		5	18.02	-0.46	7.87	18.75	13.51	10.94	11.94	-0.18	0.46	7.03	9.58	9.08	7.49	24.81
	SWIR1	3	16.82	39.55	14.13	7.78	43.59	23.16	12.20	-0.21	7.79	17.57	5.27	19.82	10.29	9.95
		4	18.55	7.29	3.73	17.46	12.53	8.42	11.11	-2.50	-3.23	-0.13	8.71	6.98	7.14	7.98
		5	17.72	-1.82	6.98	15.64	9.47	17.29	11.41	-2.44	-1.85	9.12	11.14	7.20	5.33	12.93
	SWIR2	3	16.90	42.83	13.51	7.73	44.37	17.52	11.29	6.68	8.38	17.49	5.66	30.58	12.18	10.15
		4	18.24	7.80	3.88	8.59	17.06	8.50	10.95	-4.11	-4.02	-0.40	8.97	7.00	5.28	7.47
		5	17.72	-2.09	6.49	15.73	9.63	12.40	11.36	-3.77	-3.53	10.18	9.15	7.35	6.16	18.20
	NDWI	3	18.07	13.97	11.50	15.32	23.54	8.80	11.63	7.04	8.92	11.73	9.29	8.88	6.48	9.26
		4	19.13	5.67	4.16	8.15	8.58	7.91	12.21	4.88	1.81	-1.53	11.21	9.03	9.83	11.94
		5	19.02	6.18	8.14	9.21	13.19	10.05	12.76	6.28	6.18	8.00	6.83	9.08	10.99	15.79
C 1 PIXEL LANDWARDS	NIR	3	-0.65	11.43	8.71	22.13	27.71	22.69	-4.03	6.62	7.97	8.16	10.55	17.50	14.81	12.15
		4	-2.60	7.40	14.19	27.47	6.97	13.99	-5.89	4.26	9.20	19.11	11.64	4.00	8.73	10.01
		5	12.81	5.42	12.52	22.01	21.44	23.42	7.59	1.94	6.53	16.42	10.68	10.70	13.16	31.72
	SWIR1	3	3.47	12.63	7.21	17.13	24.61	29.45	-4.80	5.04	7.50	9.04	9.92	14.09	15.39	10.66
		4	-1.28	7.17	14.51	23.37	14.84	15.06	-6.48	2.81	8.57	19.63	12.37	3.07	7.07	6.29
		5	12.29	3.57	10.77	21.94	8.12	22.07	7.16	0.13	3.05	13.57	10.12	6.87	4.45	27.56
	SWIR2	3	3.75	13.11	10.80	24.64	24.31	28.45	-5.28	3.31	7.09	8.28	12.57	14.77	16.82	14.12
		4	-0.89	7.15	14.41	23.66	14.84	16.14	-6.47	2.06	7.96	20.65	10.98	3.28	7.07	14.15
		5	11.68	3.31	9.45	14.72	7.45	20.12	7.66	-1.09	2.19	17.83	7.80	7.16	6.54	32.78
	NDWI	3	-10.58	18.95	9.04	10.40	32.52	23.84	-8.84	-2.46	10.10	4.41	12.34	37.62	18.43	13.00
		4	-9.96	11.52	14.23	21.91	6.86	14.11	-8.73	9.24	10.84	16.46	13.60	6.87	11.76	11.47
		5	13.51	9.73	12.02	15.47	16.08	14.01	8.38	6.34	10.40	9.41	10.75	11.59	10.99	20.89

Fig. 10. Mean and standard deviations values (in meters) for all the 84 different combinations analyzed changing the kernel size (K), polynomial degree (D) and input sensor band. The experiment considers 39 images of L8 and 52 images of S2. Results are obtained by using as input shoreline: (A) an accurate one, (B) synthetically displacing it seawards, and (C) displacing it landwards. The magnitude of the errors are represented by a color scale.

The displacement of the initial approximate line, both seawards and landwards (Fig. 10B and 10C respectively), affects the accuracy of the extracted shoreline increasing the errors considerably. That is especially remarkable for L8 with the displacement seawards (red tones in Fig. 10B) showing higher errors −for almost all the combinations− that even exceed the pixel size. The spatial resolution of these images along with an excessive displacement causes that most of the pixels contained in the analyzed kernel are water, which prevents the algorithm from properly detect the shoreline. On the other hand, also for S2 but especially for L8, it is observed that the landward displacement tends to cause higher values of dispersion. In this case, that is due to the presence of other elements apart from the beach surface, as vegetation or buildings, which produce a high level of heterogeneity affecting the sensitivity of the algorithm.

Looking at the solutions obtained in figures 10B and 10C for the combination of parameters previously stablished as the best one in section 4.1 (SWIR1 band, a third-degree for the polynomial adjustment and a kernel size of 3 and 5 for L8 and S2 respectively), it seems clear that conversely, with a displaced initial line, this choice would be completely unsuitable. When considering an initial line displaced seawards the extracted shorelines show errors of 16.82±7.78 m for L8 and -0.21±19.82 m for S2, and likewise, when the approximate line is displaced landward, the errors reach 3.47 ±17.13 m for L8 and 5.04±14.09 m for S2.

These results confirm that the goodness of the initial line directly affects the quality of the extracted shorelines being necessary to find a strategy which minimizes this effect.

4.3. Iterative extraction procedure

According to the previous results, working with large kernels seems an adequate strategy to avoid effects of eventual displacements and inaccuracies of the approximate line (refer to columns with large kernels in Fig. 10B and 10C). On the contrary, when the kernel of analysis is properly located, smaller kernels allow to obtain shorelines with the highest possible accuracy (Fig 10A).

An iterative strategy is proposed in order to combine the advantages of both approaches. First the algorithm runs using a large kernel following an initial approximate line. Subsequently, the resulting shoreline is taken as input for a second extraction process, in which a smaller kernel is employed. Proceeding this way, it is expected to minimize the effects that an inaccurate initial line could have on the definition of the sub-pixel shoreline.

At this point, the first question is about how to decide the optimum values of the kernel and the polynomial degree to carry out each iteration. Table 2 shows the best combination of parameters when the accuracy of the initial shoreline is sufficient being this the one to follow in the second iteration of the refining process.

Figure 11 compiles the RMSE values of the resulting SDS obtained by using the three different starting lines and for each of the 84 combinations analyzed (36 for L8 and 48 for S2 carried out in Test 1 and Test 2).

Fig. 11. Accuracy expressed in RMSE values for each combination of parameters in the x-axis (results of Test 1 and 2). B-D-K initials mean: input Band, polynomial Degree and Kernel size. Red circles identify the combination with best global behavior for all series despite the accuracy of the initial line, whereas blue circles identify the best combination in absolute terms (best sub-pixel solution).

In this sense, for L8, the combination of SWIR1 band, K=5 and D=5 presents the best results regardless the inaccuracy of the initial shoreline (red circle) assuring that the algorithm locates the shoreline in its correct position. In fact, the three solutions almost converge in the same value. Then, once this is correctly approximated, the combination of SWIR1 band, K=3 and D=3 achieves to define the shoreline with the maximum accuracy (blue circle) as Table 2 also exposed. Equivalent solutions were obtained from the images of S2 where their higher spatial resolution leads to the use of a larger but equivalent kernel. Therefore, the best global combination is SWIR1 band, K=7 and D=5 and the very best of the three series is SWIR1 band, K=5 and D=3. In this sense, these combinations are the ones proposed to be used in the iterative strategy as shown in Fig 12.

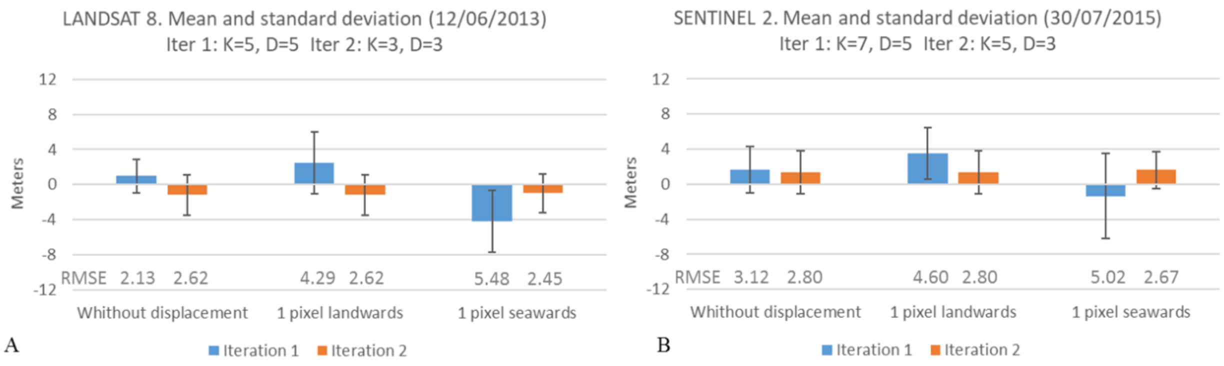

Fig. 12. Results for the iteration strategy performed for 12/06/2013 and 30/07/2015 in figures 12A and B respectively.

From the analysis of all this data, we can observe in Fig. 12 that the iterative procedure works properly in this area and the results converge with very similar RMSE values regardless of the approximate line used as input. The accuracies of the final sub-pixel shorelines reached in second iteration (orange boxes) are almost the same indifferently from working with an accurate initial shoreline or a displaced one (differences between solutions of 17 cm for 12/06/2013 in Fig 12A, and up to 13 cm for 30/07/2015 in Fig 12B). However, it is relevant to notice that stopping after the first iteration (blue boxes), the found shorelines would be wrongly detected with errors around the 5 m when the initial shore is displaced landward or seaward. Additionally, it is also important to remark that even working with an accurate approximate line, the location of the resulting shorelines is improved by about 50 cm after the second iteration (refer to left results of figures 12A and B).

Finally, in order to analyze the behavior of the algorithm when running the first iteration with a kernel even larger, another experiment was performed changing the initial conditions only for the first iteration to K=7 for L8 and K=11 for S2 (Fig. 13). The parameters for the second iteration remain the same.

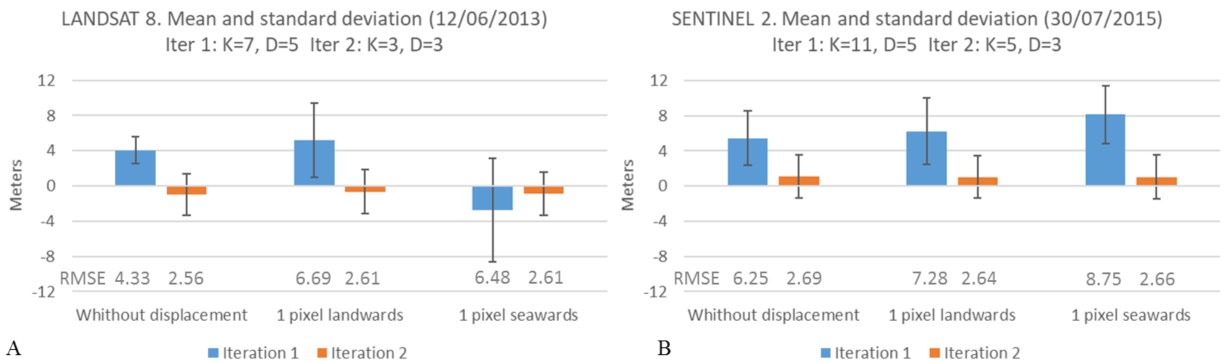

Fig. 13. Results for the iteration strategy as in Fig. 12 but running SHOREX with larger kernel size for the first iteration.

Results show that the improvement of the iterative proposal is even more remarkable when using larger kernels in the first iteration. This enforces the idea of using the iteration and ensures that regardless the inaccuracy of the initial shoreline, the algorithm is able to relocate the shoreline to their correct place through the first iteration and to define it accurately through the second one. Fig. 13 indicates that large kernels lead to wrong sub-pixel shoreline locations for the three used input lines (blue boxes in figures 13A and B) with RMSE values between 4.33 m and 8.75 m. However, the second iteration with small kernels is more than capable of obtaining an accurate SDS with an RMSE around 2.6 m (in line with the results shown in Fig. 12).

5. Discussion

This paper proposes an efficient protocol for the automatic extraction of sub-pixel shorelines reaching accuracies close to 3m RMSE on the study area, the microtidal beach of Cala Millor. The work develops several methodological improvements over previous works (Pardo-Pascual et al., 2012, Almonacid-Caballer, 2014). On the one hand, the use of a single approximate shoreline as input is key for reducing processing times by avoiding threshold methods. It enables the automation of the process eluding the only step that required user intervention and that was susceptible to generate discontinuities and uncertainties at the pixel level. On the other hand, the method presents an improvement in robustness by incorporating an iterative extraction step, shifting from larger to smaller kernels. This iteration assures high precisions in the detection of the final shoreline even with an approximate input line eventually displaced. It may occur as the shoreline position is expected to experience changes along time associated with differences in the tidal level, energy of the incident waves and their associated excursions, and the morphology of the intertidal zone. These improvements result in a workflow efficient enough to successfully cope with the definition of shorelines at the same rate the L8 and S2 images are acquired.

The implementation of the entire workflow within a single integrated system is also essential for gaining efficiency. SHOREX has been conceived as a complete system that includes all the necessary phases to obtain the final sub-pixel SDS: image download, subdivision into manageable spatial units and homogenization of their characteristics, supervision of cloud coverage, sub-pixel georeferencing, sub-pixel extraction of the shoreline to point format, elimination of outliers and transformation of the result into linear format. Currently, all these processes can be performed automatically (with the exception of the optional cloud checking, with a user-friendly visualization tool completely integrated into the process).

The efficiency of the extraction protocol and its limiting factors are in line with previous works (Palomar-Vázquez et al., 2018a, b), in which the downloading was the most time-consuming phase.

The accuracy and precision of the obtained shorelines is a second key aspect in order to determine their usefulness in coastal change studies. However, to carry out a thorough assessment is not simple and relatively few studies (e.g. García-Rubio et al., 2015, Liu et al., 2017b, Splinter et al., 2018, Pardo-Pascual et al., 2018, Hagenaars et al., 2018, Do et al., 2019, Vos et al., 2019a) have made a metric evaluation of the errors. This is largely due to the difficulty of recording the shoreline position with sufficient precision at the same instant the image is captured by satellite.

In the present study, video-derived shorelines have been obtained simultaneously to the acquisition of the satellite images, and processed and converted to georectifed images by applying C-Pro (Sánchez-García et al., 2017) with a 1.54 m RMSE. However, the accuracy of the digitalized shoreline on these images was also conditioned by the criterion and audacity of the interpreter, as well as the indeterminacy of the spatial resolution of the georectified image. At a distance of 650 m and for the worst cases, working with a focal of 1332 pixels, the cross and long size of the pixel footprint have been 0.45 m and 6.36 m respectively. Despite these errors, the video-derived shorelines are amply valid to be used as reference data. Pardo-Pascual et al., (2018) already validated these video-derived shorelines obtained with C-Pro in a sector of the Valencian coast by comparing them against shorelines simultaneously measured by GPS, showing an encouraging mean error of 0.15 ±1.05 m.

In the present work, the large number of evaluations (91) ensures that different oceanographic conditions have been considered (relative to a microtidal environment), giving high robustness to the results. Testing the combination of different extraction parameters have made it possible to identify those that provide the highest accuracy (Table 2) −reaching values even close to those inherent of the reference/video-derived data. Moreover, when using more demanding quality indicators such as the 5th and 95th percentiles, 90% of the errors range between -5.1 to 5.9 m for L8, and between -2.9 to 5.4 m for S2. Likewise, for each particular date (Fig. 14) in the vast majority of cases it has been observed that the errors were within the described margins. In fact, the maximum average error was 3.2 m and the minimum was -3.7 m. The standard deviation was also mainly maintained close to 2.5 m.

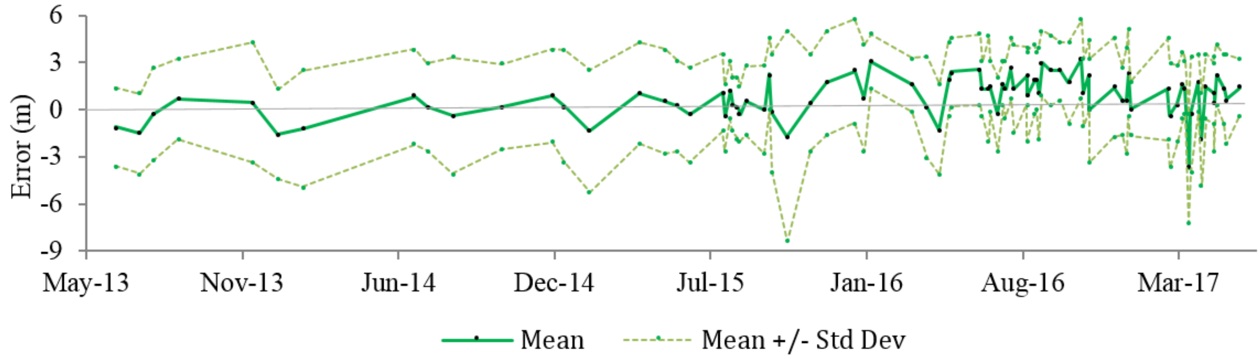

Fig. 14. Range of errors (mean ± standard deviation) of the 91 SDS analyzed over the 4-year study.

Extreme values in the standard deviation (such as 6.7 m for 21/10/2015) appeared on days in which wave conditions show high run-up. As the instant of the capture of the satellite image and the video-camera did not completely coincide, a significant error appeared in some parts of the beach. As Fig. 15 shows for this particular day, it is interesting to observe how at the locations where the SDS is more distant to the video-derived shoreline (greater errors), the S2 shoreline is identifying a clear humidity line, probably because of getting wet very recently. It was precisely those days the ones that recorded the highest waves (Hs = 1.35 m, Tp = 9.35 sec) of the entire series. However, and despite knowing that higher waves may lead to errors in the detection of the shoreline (Hagenaars et al., 2018), in the current work it is found a different effect to the one observed in Pardo-Pascual et al. (2018). That time, with a very similar algorithmic solution and a 7x7 kernel, the wave conditions directly affected the shoreline bias (especially the wavelength and wave period). On the contrary, in this study the comparison between the errors of the SDS and the wave characteristics has shown a practically null relation (r^2=0.044 and r^2=0.025 with respect to the wave period and, r^2=0.051 and r^2=0.046 with respect to the height of the incident waves, respectively for L8 and S2). This may be due to the fact that Pardo-Pascual et al., 2018 worked with thresholding initial shorelines which were more easily confused with other wave breaking lines and so the algorithm was not able to reach a final accurate position. However, the methodology presented in the current paper (starting with a unique approximate line and following with an iterative process) is being generally less influenced by these external factors or is otherwise able to overcome them.

The results evidence a substantial improvement in the level of accuracy with respect to previous solutions described in the bibliography for microtidal and moderately energetic coastal areas where SDS have been compared with field measurements. For instance, Hagenaars et al. (2018) obtained an average error for L8 and S2 images of 9.5 (±16 m) and 10.5 (±12 m) in a coastal segment of around 1.7 m tide; Liu et al. (2017b) reported about 10 m RMSE at a beach with 2 m tide; and more recently, Vos et al. (2019a) reached accuracies ranging from 7.2 m to 11.6 m RMSE on four microtidal beaches of Australia, New Zealand and USA.

In agreement with Almonacid-Caballer et al. (2016), Liu et al. (2017b) remarked that the shorelines obtained from Landsat images (using an algorithmic solution different from the one exposed in this work) were adequate to monitor the average annual behavior of the beaches, but they could be subjected to excessively large errors (tens of meters). Hagenaars et al. (2018) have recently suggested applying image composite processing −following Donchyts et al., 2016 technique− to a sequence of images in order to obtain a single image that minimizes the effect of bias factors. It is shown that even dealing with relatively high errors (within 15 m RMSE) the study of evolutionary trends over large coastal segments is possible (Sánchez-García et al., 2015; Almonacid-Caballer et al., 2016; Do et al., 2019, Cabezas-Rabadán et al., 2019b, Vos et al., 2019a) and also on a global scale as proposed by Luijendijk et al. (2018) and Mentaschi et al. (2018).

SHOREX system, with the methodology and accuracy here shown, resolves the limitation of low resolution and opens up the possibility of using the SDS in analytical processes that require greater precision. The methodology makes it possible to offer continuous data throughout the year, with a high revisited frequency of wide coastal segments allowing to derive useful indicators for coastal management as the beach width (Cabezas-Rabadán et al., 2019a), to estimate volumetric changes on certain beach profiles (Do et al., 2019) and to monitor the beach along sub-annual periods (Vos et al., 2019 a) as the response to nourishment projects or coastal storms (Cabezas-Rabadán et al., 2019b; Pardo-Pascual et al., 2014). Nevertheless, for all these purposes it seems reasonable to relate the defined water/land border with an elevation value that is strongly influenced by sea-level variations (Boak and Turner, 2005; Kabuth et al., 2014). Only this way SDS would constitute a valid indicator of shoreline changes.

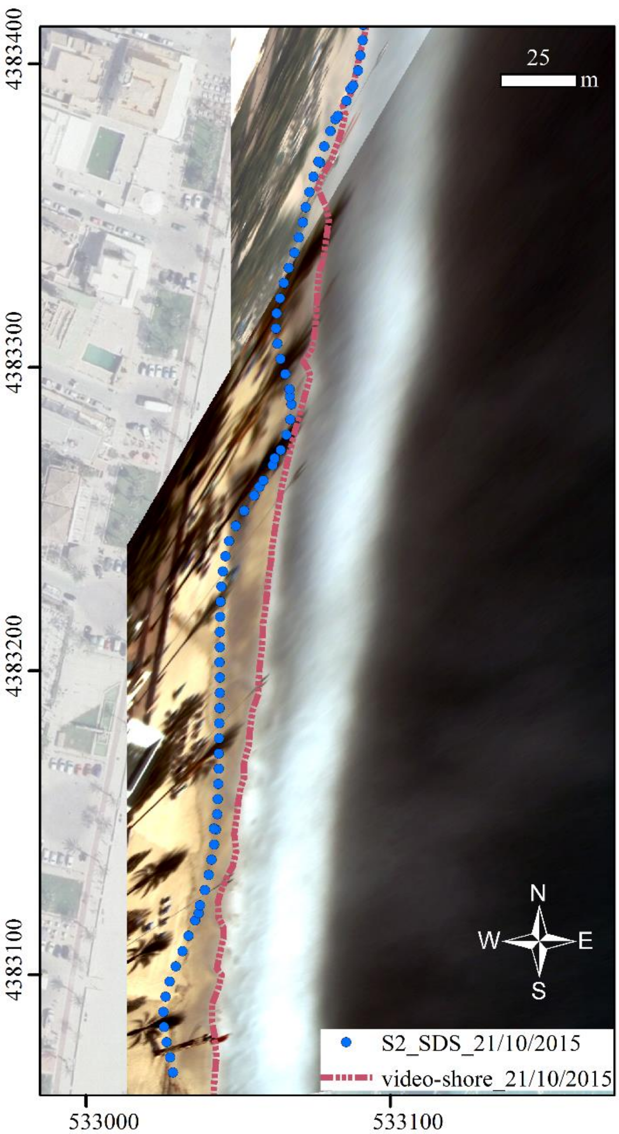

Fig. 15. Comparison of the shoreline obtained from S2 (SWIR1 band) using SHOREX and the video-derived shoreline for 21/10/2015, the day in which the highest waves were registered.

The application of the extracted SDS for monitoring purposes is immediate on microtidal beaches as the wet zone is rarely very wide. However, in beaches with high variations in tide and wave conditions this solution would need to be re-evaluated as is expected that the interaction with these factors make the definition of the land-water border and the association with its elevation more difficult. In meso or macrotidal coasts, the shoreline definition can be compromised due to larger run-up excursions, as well as in areas with very low slopes and high tidal range, where the intertidal space can be extended to hundreds of meters. In these cases, and following the iterative procedure here described, the use of an approximate line could cause that the kernel of 7 x 7 pixels for the first iteration did not include the position of the real shoreline, making insufficient the proposed iterative protocol. The solution could come from the definition of different approximate lines associated with different sea levels, the performance of consecutive iterations starting from larger kernels of analysis, or the synergy with a new image interpolation method (Sánchez-García et al., 2019a) where the land-water surface is modeled by a piecewise interpolating polynomial that adapts to the maximum radiometric variations. Anyways, future research is required to continue testing SHOREX on a wide miscellany of coastal environments and achieve its full automation on a large spatial scale.

6. Conclusions

The present work proposes an efficient protocol for shoreline extraction from mid-resolution satellite images using the SHOREX system. A workflow that integrates all the necessary steps for an automatic definition of the shoreline position at sub-pixel level has been described, increasing both the efficiency and the accuracy of the extraction. The protocol allows the massive definition of shorelines at the same rate as the acquisition of satellite images. This is of great value for the continuous monitoring of beaches and the decision-making of coastal managers.

The assessment of a large set of SDS (91) over almost 4 years has been carried out in Cala Millor, a Mediterranean sandy beach. This was possible thanks to the availability of highly accurate shorelines from a video-monitoring system in the same instant the satellite images were recorded. The evaluation has allowed analyzing 84 different combinations of parameters for working with SHOREX by merging the type of input band, the kernel of analysis and adjustment degree. Accordingly, it was possible to establish that the combination leading to the best solution (an RMSE of 3.57 m for L8 and 3.01 m for S2) was using the SWIR1 band, a third-degree polynomial, and a 3x3 kernel size for L8 and 5x5 for S2 (equivalent kernel according to the different spatial resolution). Moreover, the results showed that the accuracy of the input line strongly affects the final sub-pixel shoreline definition. Therefore, an iterative strategy using

SHOREX was proposed to minimize this effect and ensuring a robust method for shoreline detection regardless of the reliability of the input line and external factors.

The high availability of satellite-image data worldwide together with the efficiency and accuracy of SHOREX creates a new scenario and an opportunity to understand the morphodynamics of coastal zones on different spatio-temporal scales.

Acknowledgments

This study is supported by the grants of E. Sánchez-García (FPU13/05877) and C. Cabezas-Rabadán (FPU15/04501) from the Spanish Ministry of Education, Culture and Sports, as well as the project RESETOCOAST (CGL2015-69906-R) from the Spanish Ministry of Economy and Competitiveness. Authors also acknowledge SOCIB (MICINN-CAIB) for providing video-monitoring images and sea level tide gauge records.

References

Aarninkhof, S.G., Turner, I.L., Dronkers, T.D.T., Caljouw, M., Nipius, L., 2003. A video-based technique for mapping intertidal beach bathymetry. Coast. Eng. 49, 275–289. https://doi.org/10.1016/S0378-3839(03)00064-4.

Addo, K. A., Jayson-Quashigah, P. N., & Kufogbe, K. S., 2011. Quantitative analysis of shoreline change using medium resolution satellite imagery in Keta, Ghana. Marine Science, 1(1), 1-9. https://doi.org/10.5923/j.ms.20110101.01.

Aedla, R., Dwarakish, G.S., Venkat R.D., 2015. Automatic shoreline detection and change detection analysis of Netravati-GurpurRivermouth using histogram equalization and adaptive thresholding techniques. Aquatic Procedia 4(0):563–570. https://doi.org/10.1016/j.aqpro.2015.02.073.

Alharbi, O. A., Phillips, M. R., Williams, A. T., Thomas, T., Hakami, M., Kerbe, J., Al-Ghamdi, K., 2017. Temporal shoreline change and infrastructure influences along the southern Red Sea coast of Saudi Arabia. Arabian Journal of Geosciences, 10(16), 360. https://doi.org/10.1007/s12517-017-3109-7.

Almonacid-Caballer, J., 2014. Extraction of Shorelines with Sub-Pixel Precision from Landsat Images (TM, ETM+, OLI) [Obtención de Lineas de Costa con Precisión Sub-Pixel a Partir de Imágenes Landsat (TM, ETM+ y OLI)]. Ph.D. Thesis, Universitat Politècnica de València, Valencia, Spain.

Almonacid-Caballer, J., Sánchez-García, E., Pardo-Pascual, J.E., Balaguer-Beser, A.A., Palomar-Vázquez, J., 2016. Evaluation of annual mean shoreline position deduced from Landsat imagery as a mid-term coastal evolution indicator. Mar. Geol. 372, 79–88. https://doi.org/10.1016/j.margeo.2015.12.015.

Almonacid-Caballer, J., Pardo-Pascual, J.E., Ruiz, L.A., 2017. Evaluating fourier cross-correlation sub-pixel registration in Landsat images. Remote Sens. 9. https://doi.org/10.3390/rs9101051.

Álvarez-Ellacuría, A., Orfila, A., Gómez-Pujol, L., Simarro, G., Obregón, N., 2011. Decoupling spatial and temporal patterns in short-term beach shoreline response to wave climate. Geomorphology 128, 199-208. https://doi.org/10.1016/j.geomorph.2011.01.008.

Boak, E.H., Turner, I.L., 2005. Shoreline Definition and Detection: A Review. Journal of Coastal Research 21-4, 688–703.

Bouguet, J.Y., 2015. Camera Calibration Toolbox for Matlab. Available at: <http:// www.vision.caltech.edu/bouguetj/calib_doc/>.

Brignone, M., Schiaffino, C.F., Isla, F.I., Ferrari, M., 2012. A system for beach video-monitoring: Beachkeeper plus. Comput. Geosci. 49, 53–61. https://doi.org/10.1016/j.cageo.2012.06.008.

Cabezas-Rabadán, C., Pardo-Pascual, J.E., Palomar-Vázquez, J., Almonacid-Caballer, J., Fernández-Sarría, A., 2018. La posición de la línea de costa extraída de imágenes satelitales como herramienta de seguimiento y análisis de cambios en playas mediterráneas. XVIII Congreso Nacional de Tecnologías de La Información Geográfica (TIG). Dept. Geografia. Universitat de València, València, pp. 36–46.

Cabezas-Rabadán, C., Pardo-Pascual, J.E., Almonacid-Caballer, J., and Rodilla, M., 2019a. Detecting problematic beach widths for the recreational function along the Gulf of Valencia (Spain) from Landsat 8 subpixel shorelines. *Applied Geography*, 110, 102047.

Cabezas-Rabadán, C., Pardo-Pascual, J.E., Palomar-Vázquez, J. M., and Fernández-Sarría, A., 2019b. Characterizing beach changes using high-frequency Sentinel-2 derived shorelines on the Valencian coast (Spanish Mediterranean). *Science of the Total Environment*, 691, 216-231.

Choung, Y.J. & Jo, M.H., 2015. Shoreline change assessment for various types of coasts using multi-temporal Landsat imagery of the east coast of South Korea. Remote Sens. Lett., 7, 91-100. https://doi.org/10.1080/2150704X.2015.1109157.

Clerc, S. MPC Team. S2 MPC. Data quality report, 2017, reference S2-PDGS-MPC-DQR, issue 20. https://sentinels.copernicus.eu/documents/247904/685211/Sentinel-2-Data-Quality-Report.

Davidson, M., Van Koningsveld, M., de Kruif, A., Rawson, J., Holman, R., Lamberti, A., Medina, R., Kroon, A., Aarninkhof, S., 2007. The CoastView project: Developing video-derived Coastal State Indicators in support of coastal zone management. Coast. Eng. 54, 463–475. https://doi.org/10.1016/j.coastaleng.2007.01.007.

Do, A.T.K.; de Vries, S., and Stive, M.J.F., 2019. The estimation and evaluation of shoreline locations, shoreline-change rates, and coastal volume changes derived from Landsat images. *Journal of Coastal Research*, 35(1), 56–71. https://doi.org/10.2112/JCOASTRES-D-18-00021.1.

Donchyts, G., Baart, F., Winsemius, H., Gorelick, N., Kwadijk, J., van de Giesen, N., 2016. Earth's surface water change over the past 30 years. Nat. Clim. Change 6, 810–813.

Enríquez, A.R., Marcos, M., Álvarez-Ellacuría, A., Orfila, A., Gomis, D. 2017. Changes in beach shoreline due to sea level rise and waves under climate change scenarios: application to the Balearic Islands (western Mediterranean). Nat. Hazards Earth Syst. Sci., 17, 1075-1089, https://doi.org/10.5194/nhess-17-1075-2017, 2017.

Esteves, L. S., Williams, J. J., Nock, A., & Lymbery, G., 2009. Quantifying shoreline changes along the Sefton coast (UK) and the implications for research-informed coastal management. Journal of Coastal Research, SI 56 (Proceedings of the 10th Int. Coastal Symposium), 602-606. Lisbon, Portugal, ISSN 0749-0258.

Feyisa, G. L., Meilby, H., Fensholt, R., Proud, S. R., 2014. Automated Water Extraction Index: A new technique for surface water mapping using Landsat imagery. Remote Sens. Environ., 140, 23–35. https://doi.org/10.1016/j.rse.2013.08.029.

Foody, G.M., Muslim, A.M., Atkinson, P.M., 2005. Super-resolution mapping of the waterline from remotely sensed data. Int. J. Remote Sens., 26(24), 5381-5392, https://doi.org/10.1080/01431160500213292.

Ford, M., 2013. Shoreline changes interpreted from multi-temporal aerial photographs and high resolution satellite images: Wotje Atoll, Marshall Islands. Remote Sensing of Environment, 135, 130–140. https://doi.org/10.1016/j.rse.2013.03.027.

Frazier, P.S. & Page, K.J., 2000. Water Body Detection and Delineation with Landsat TM Data. Photogramm. Eng. Remote Sens. 66, 1461–1467. https://doi.org/0099-1112I0OI6612-1461$3.00/0.

García-Rubio, G., Huntley, D., Russell, P., 2015. Evaluating shoreline identification using optical satellite images, Marine Geology 359, 96-105. https://doi.org/10.1016/j.margeo.2014.11.002.

Gómez-Pujol, L., Orfila, A., Álvarez-Ellacuría, A., Tintoré, J., 2011. Controls on sediment dynamics and medium-term morphological change in a barred microtidal beach (Cala Millor, Mallorca, Western Mediterranean). Geomorphology 132, 87-98. https://doi.org/10.1016/j.geomorph.2011.04.026.

Gómez-Pujol, L., Orfila, A., Cañellas, B., Álvarez-Ellacuría, A., Méndez, F.J., Medina, R. and Tintoré, J., 2007. Morphodynamic classification of sandy beaches in low energetic marine environment. Marine Geology 242, 235-246. https://doi.org/10.1016/j.margeo.2007.03.008.

Gomis, D., Tsimplis, M., Marcos, M., Fenoglio-Marc, L., Pérez, B., Raicich, F., Vilibic, I., Wöppelmann, G., Montserrat, S., 2012. Mediterranean sea-level variability and trends. In: Lionello, P. (ed.) The climate of Mediterranean region: from the past to the future, 257-299. https://doi.org/10.1016/B978-0-12-416042-2.00004-5.

Graham, R. L. & Hell, P., 1985. On the history of the minimum spanning three problem. IEEE Annals of the History of Computing, 7, 43-57. https://doi.org/10.1109/MAHC.1985.10011.

Guizar-Sicairos, M.; Thurman, S.T.; Fienup, J.R., 2008. Efficient subpixel image registration algorithms. Opt. Lett., 3, 156–158.

Hagenaars, G., de Vries, S., Luijendijk, A., de Boer, W. P. & Reniers, A.J.H.M., 2018. On the accuracy of automated shoreline detection derived from satellite imagery: a case study of the Sand Motor mega-scale nourishment, Coastal Engineering, 133: 113-125 https://doi.org/10.1016/j.coastaleng.2017.12.011.

Infantes, E., Orfila, A., Terrados, J., Luhar, M., Nepf, H., 2012. Effect of a seagrass (Posidonia oceanica) meadow on wave propagation. Marine Ecology Progress Series 456, 63-72. http://doi.org/10.3354/meps09754.

Iron, J.R., Dwyer, J.L., Barsi, J.A., 2012. The next Landsat satellite: The Landsat Data Continuity Mission. Remote Sens. Environ., 122, 11-21. http://doi.org/10.1016/j.rse.2011.08.026.

Ji, L., Zhang, L., &Wylie, B., 2009. Analysis of dynamic thresholds for the normalized difference water index. Photogrammetric Engineering and Remote Sensing, 75, 1307–1317. https://doi.org/10.14358/PERS.75.11.1307.

Jones, B. M., Arp, C. D., Jorgenson, M. T., Hinkel, K. M., Schmutz, J. A., & Flint, P. L., 2009. Increase in the rate and uniformity of coastline erosion in Arctic Alaska. Geophysical Research Letters, 36(3). https://doi.org/10.1029/2008GL036205.

Kabuth, A.K., Kroon, A., Pedersen, J.T.P., 2014. Multi-decadal shoreline changes in Denmark. *Journal of Coastal Research* 30-4, 714-728.

Li, J. & Roy, D.P., 2017. A global analysis of Sentinel-2a, Sentinel-2b and Landsat 8 data revisit intervals and implications for terrestrial monitoring. Remote Sens., 9, 902. https://doi.org/10.3390/rs9090902

Li, L., Chen, Y., Xu, T., Liu, R., Shi, K., Huang, C., 2015. Super-resolution mapping of wetland inundation from remote sensing imagery based on integration of back-propagation neural network and genetic algorithm. Remote Sens. Environ., 164, 142-154, doi: https://doi.org/10.1016/j.rse.2015.04.009.

Li, X. & Damen, M.C.J., 2010. Coastline change detection with satellite remote sensing for environmental management of the Pearl River Estuary, China, Journal of Marine Systems, 82: 554-561. https://doi.org/10.1016/j.jmarsys.2010.02.005.

Li, W. & Gong, P., 2016. Continuous monitoring of coastline dynamics in western Florida with a 30-year time series of Landsat imagery. Remote Sens. Environ. 179: 196–209. https://doi.org/10.1016/j.rse.2016.03.031.

Liu, H., Wang, L., Sherman, D.J., Wu, Q., Su, H., 2011. Algorithmic Foundation and Software Tools for Extracting Shoreline Features from Remote Sensing Imagery and LiDAR Data. J. Geogr. Inf. Syst. 03, 99–119. https://doi.org/10.4236/jgis.2011.32007.

Liu, Q., Trinder, J., Turner, I.L., 2017b. Automatic super-resolution shoreline change monitoring using Landsat archival data: a case study at Narrabeen–Collaroy Beach, Australia. J. Appl. Remote Sens. 11, 016036. https://doi.org/10.1117/1.JRS.11.016036.

Liu, Y., Wang, X., Ling, F., Xu, S., Wang, C., 2017a. Analysis of coastline extraction from Landsat-8 OLI imagery. Water (Switzerland) 9, 1–26. https://doi.org/10.3390/w9110816.

Luijendijk, A., Hagenaars, G., Ranasinghe, R., Baart, F., Donchyts, G., & Aarninkhof, S., 2018. The state of the world's beaches, Scientific Reports, 8: 6641. https://doi.org/10.1038/s41598-018-24630-6.

Maiti, S. & Bhattacharya, A.K., 2009. Shoreline change analysis and its application to prediction: A remote sensing and statistics based approach. Mar. Geol. 257, 11–23. https://doi.org/10.1016/j.margeo.2008.10.006.

McFeeters, S. K., 1996. The use of the Normalized Difference Water Index (NDWI) in the delineation of open water features, International Journal of Remote Sensing, 17:7, 1425-1432. https://doi.org/10.1080/01431169608948714.

Mentaschi, L., Vousdoukas, M. I., Pekel, J. F., Voukouvalas, E., & Feyen, L., 2018. Global long-term observations of coastal erosion and accretion. Scientific Reports, 8(1), 1–11.

Mills, J. P., Buckley, S. J., Mitchell, H. L., Clarke, P. J., & Edwards, S. J., 2005. A geomatics data integration technique for coastal change monitoring. Earth Surface Processes and Landforms: The Journal of the British Geomorphological Research Group, 30(6), 651-664. https://doi.org/10.1002/esp.1165.

Morton, R. A., Miller, T. L., Moore, L. J., 2004, National assessment of shoreline change: Part 1: Historical shoreline changes and associated coastal land loss along the U.S. Gulf of Mexico: U.S. Geological Survey Open-file Report 2004-1043, 45p. https://doi.org/10.3133/ofr20041043.

Nieto, M. A., Garau, B., Balle, S., Simarro, G., Zarruk, G. A., Ortiz, A., Tintoré, J., Álvarez-Ellacuría, Gómez-Pujol, L., Orfila, A., 2010. An open source, low cost video-based coastal monitoring system. Earth Surf. Process. Landforms 35, 1712–1719. https://doi.org/10.1002/esp.2025.

Osorio, A., Medina, R., Gonzalez, M., 2012. An algorithm for the measurement of shoreline and intertidal beach profiles using video imagery: PSDM. Computers & Geosciences, 46, 196-207. doi:10.1016/j.cageo.2011.12.008.Ouma, Y.O. & Tateishi, R., 2006. A water index for rapid mapping of shoreline changes of five East African Rift Valley lakes: An empirical analysis using Landsat TM and ETM+ data. Int. J. Remote Sens., 27, 3153–3181. https://doi.org/10.1080/01431160500309934.

Pajak, M. J., & Leatherman, S., 2002. The high water line as shoreline indicator. Journal of Coastal Research, 329-337.

Palomar-Vázquez, J.M., Almonacid-Caballer, J., Pardo-Pascual, J.E., Sánchez-García, E., 2018a. SHOREX: a new tool for automatic and massive extraction of shorelines from Landsat and Sentinel 2 imagery. Proceedings of the 7th International Conference on the Application of Physical Modelling in Coastal and Port Engineering and Science (Coastlab18), 22-26 May, Santander.

Palomar-Vázquez, J.M., Almonacid-Caballer, J., Pardo-Pascual, J.E., Cabezas-Rabadán, C., Fernández-Sarría, A., 2018b. Sistema para la extracción masiva de líneas de costa a partir de imágenes satélite de resolución media para la monitorización costera: SHOREX. Perspectivas multidisciplinares en la sociedad del conocimiento. XVIII Congreso de Tecnologías de la Información Geográfica, pp. 25-35, València.

Pardo-Pascual, J., García-Asenjo, L., Palomar-Vázquez, J., & Garrigues-Talens, P., 2005. New methods and tools to analyze beach-dune system evolution using a Real-Time Kinematic Global Positioning System and Geographic Information Systems. Journal of Coastal Research, (Special Issue 49), 34-39.

Pardo-Pascual, J.E., Almonacid-Caballer, J., Ruiz, L. A., Palomar-Vázquez, J., 2012. Automatic extraction of shorelines from Landsat TM and ETM+ multi-temporal images with subpixel precision. Remote Sens. Environ. 123, 1–11. https://doi.org/10.1016/j.rse.2012.02.024.

Pardo-Pascual, J. E., Almonacid-Caballer, J., Ruiz, L. A., Palomar-Vázquez, J., and Rodrigo-Alemany, R., 2014. Evaluation of storm impact on sandy beaches of the Gulf of Valencia using Landsat imagery series. Geomorphology, 214, 388-401.

Pardo-Pascual, J.E., Sánchez-García, E., Almonacid-Caballer, J., Palomar-Vázquez, J.M., de los Santos, E.P., Fernández-Sarría, A., Balaguer-Beser, A., 2018. Assessing the accuracy of automatically extracted shorelines on microtidal beaches from Landsat 7, Landsat 8 and Sentinel-2 imagery. Remote Sens. 10. https://doi.org/10.3390/rs10020326.

Psuty, N. P. & Silveira, T. M., 2011. Tracking Coastal Geomorphological Change: an application of protocols to collect geotemporal data sets at the national level in the US. Journal of Coastal Research, (64), 1253–1257.

Quang Tuan, N.; Cong Tin, H.; Quang Doc, L.; Anh Tuan, T., 2017. Historical monitoring of shoreline changes in the Cua Dai Estuary, Central Vietnam using multi-temporal remote sensing data. Geosciences, 7, 72. https://doi.org/10.3390/geosciences7030072.

Rokni, K., Ahmar, A., Selemat, A. & Sharifeh, H., 2014. Water feature extraction and change detection using multitemporal Landsat imagery, Remote Sensing, 6 (5): 4173-4189, https://doi.org/10.3390/rs6054173.

Ruiz de Alegria-Arzaburu, A., Masselink, G., 2010. Storm response and beach rotation on a gravel beach, Slapton Sands, U.K. Marine Geology, 278(1-4), 77-99. doi:10.1016/j.margeo.2010.09.004.

Ryu, J. H., Won, J. S., Min, K. D., 2002. Waterline extraction from Landsat TM data in a tidal flat: A case study in Gomso Bay, Korea. Remote Sens. Environ., 83, 442–456. https://doi.org/10.1016/S0034-4257(02)00059-7.

Sánchez-García, E., Pardo-Pascual, J.E., Balaguer-Beser, A., Almonacid-Caballer, J., 2015. Analysis of the shoreline position extracted from Landsat TM and ETM+ imagery. International Archives of Photogrammetry, Remote Sensing and Spatial Information Sciences, 991–998. https://doi.org/10.5194/isprsarchives-XL-7-W3-991-2015.

Sánchez-García, E., Balaguer-Beser, A., Pardo-Pascual, J.E., 2017. C-Pro: A coastal projector monitoring system using terrestrial photogrammetry with a geometric horizon constraint. ISPRS J. Photogramm. Remote Sens. 128, 255–273. https://doi.org/10.1016/j.isprsjprs.2017.03.023.

Sánchez-García, E., Balaguer-Beser, A., Almonacid-Caballer, J., Pardo-Pascual, J.E., 2019a. A new adaptive image interpolation method to define the shoreline at sub-pixel level. *Remote Sens*. 11, 1880.

Sánchez-García, E., Briceño, I., Palomar-Vázquez, J., Pardo-Pascual, J., Cabezas-Rabadán, C., Balaguer-Beser, A., 2019b. Beach monitoring project on central Chile. 5ª Conferência sobre Morfodinâmica Estuarina e Costeira (MEC2019). Lisboa, Portugal; 24-25 June, 2019. ISBN: 978-989-20-9612-4; pp. 49-50.

Simarro, G., Ribas, F., Álvarez, A., Guillén, J., Chic, Ò., Orfila, A., 2017. ULISES: An Open Source Code for Extrinsic Calibrations and Planview Generations in Coastal Video Monitoring Systems. J. Coast. Res. 335, 1217–1227. https://doi.org/10.2112/JCOASTRES-D-16-00022.1.

Song, Y., Liu, F., Ling, F., and Yue, L., 2019. Automatic semi-global artificial shoreline subpixel localization algorithm for Landsat imagery. Remote Sensing, 11(15), 1779.

Splinter, K.D., Harley, M.D. & Turner, I.L., 2018. Remote sensing is changing our view of the coast: insights form 40 years of monitoring at Narrabeen-Collaroy, Australia, Remote Sensing, 10(11), 1744. https://doi.org/10.3390/rs10111744.

Taborda, R. & Silva, A., 2012. COSMOS: A lightweight coastal video monitoring system. Comput. Geosci. 49, 248–255. https://doi.org/10.1016/j.cageo.2012.07.013.

Tintoré, J. et al. 2013. SOCIB: The Balearic Islands Coastal Ocean Observing and Forecasting System Responding to Sciene, Technology and Society Needs. Marine Technology Society Journal 47, 1-17.

https://doi.org/10.4031/MTSJ.47.1.10.

Tintoré, J., Medina, R., Gómez-Pujol, L., Orfila, A., Vizoso, G., 2009. Integrated and interdisciplinary approach to coastal management. Ocean Coastal Management 52, 493-505.

Valentini, N., Saponieri, A., Molfetta, M. G., Damiani, L., 2017. New algorithms for shoreline monitoring from coastal video systems. Earth Science Informatics, 10(4), 495-506. doi:10.1007/s12145-017-0302-x.

Viaña-Borja, S. P., Ortega-Sánchez, M., 2019. Automatic methodology to detect the coastline from Landsat images with a new water index assessed on three different Spanish Mediterranean deltas. Remote Sensing, 11(18), 2186.

Vos, K., Harley, M.D., Splinter, K.D., Simmons, J.A., and Turner, I.L., 2019a. Sub-annual to multi-decadal shoreline variability from publicly available satellite imagery. *Coastal Engineering*, 150, 160-174.

Vos, K., Splinter, K.D., Harley, M.D., Simmons, J.A., & Turner, I.L., 2019b. CoastSat: a Python toolkit to extract shorelines from publicly available satellite imagery. *Environmental Modelling and Software*, 122, 104528.

Wang, C.L.; Zhao, C.X.; Yang, J.Y., 2011. Local upsampling Fourier transform for high accuracy image rotation estimation. Adv. Mater. Res., 268–270, 1488–1593. https://doi.org/10.4028/www.scientific.net/AMR.268-270.1488.

Xu, N., 2018. Detecting Coastline Change with All Available Landsat Data over 1986 – 2015 : A Case Study for the State of Texas, USA. https://doi.org/10.3390/atmos9030107.

Yamano, H., Shimazaki, H., Matsunaga, T., Ishoda, A., McClennen, C., Yokoki, H., Fujita, K., Osawa, Y., Kayanne, H., 2006. Evaluation of various satellite sensors for waterline extraction in a coral reef environment: Majuro Atoll, Marshall Islands. Geomorphology 82, 398–411. https://doi.org/10.1016/j.geomorph.2006.06.003.

Zhang, Y. & Chen, S.L., 2010. Super-resolution mapping of coastline with remotely sensed data and geostatistics. J. Remote Sens., 14, 148–164.